Small

NANO · MICRO small
www.small-journal.com

RESEARCH ARTICLE

Direct Regeneration of Spent $LiFePO_4$ Using Methionine for Defect Repair and N/S-Doped Interface Construction

Xutao Liang[1] | Ran Wang[1] | Bo Zhang[1] | Lifeng Hou[1] | Shi Wang[2] | Bing Wu[3] | Zhong Jin[4] | Qian Wang[1]

[1]College of Materials Science and Engineering, Taiyuan University of Technology, Taiyuan, Shanxi, China | [2]State Key Laboratory of Organic Electronics & Information Displays (SKLOEID), Institute of Advanced Materials (IAM), Nanjing University of Posts & Telecommunications, Nanjing, China | [3]China Coal Technology & Engineering Group (CCTEG), Chinese Institute of Coal Science (CICS), Beijing, China | [4]State Key Laboratory of Coordination Chemistry, MOE Key Laboratory of Mesoscopic Chemistry, MOE Key Laboratory of High Performance Polymer Materials and Technology, Jiangsu Key Laboratory of Advanced Organic Materials, Suzhou Key Laboratory of Green Intelligent Manufacturing of New Energy Materials and Devices, Tianchang New Materials and Energy Technology Research Center, Institute of Green Chemistry and Engineering, School of Chemistry and Chemical Engineering, Nanjing University, Nanjing, China

Correspondence: Shi Wang (iamshiwang@njupt.edu.cn) | Bing Wu (wu-b15@tsinghua.org.cn) | Zhong Jin (zhongjin@nju.edu.cn) | Qian Wang (qianwang0825@pku.edu.cn)

Received: 13 May 2026 | **Revised:** 7 July 2026 | **Accepted:** 20 July 2026

Keywords: direct regeneration | interface | $LiFePO_4$ | N/S-doped

ABSTRACT

The coming wave of end-of-life electric vehicles presents a formidable challenge for the recycling of spent Li-ion batteries, particularly those with $LiFePO_4$ cathodes. The degradation of the $LiFePO_4$ cathode is primarily attributed to Li loss-induced lattice defects and the formation of Fe(III) phase. Traditional recycling methods are often plagued by high energy consumption, environmental pollution, and low economic value. Herein, we propose a targeted direct regeneration strategy using methionine as a multifunctional reducing agent to simultaneously repair bulk crystal defects and construct a N/S-doped interface. Methionine acts as an efficient reductant, facilitating the reduction of Fe(III) to Fe(II) and the elimination of Fe-Li anti-site defects, thereby reconstructing rapid the Li^+ diffusion pathways. Simultaneously, it can serve as a single-source precursor for in situ formation of a N/S-doped carbon coating during subsequent annealing. This multifunctional interface not only significantly enhances electronic conductivity but also stabilizes the crystal structure. As a result, the regenerated $LiFePO_4$ (R-LFP) exhibits a high discharge capacity of 150.76 mAh g^{-1} at 1.0 C and outstanding cycling stability with >87% capacity retention after 800 cycles, a performance comparable to commercial LFP. This work provides an efficient and sustainable solution for the upcycling of spent Li-ion battery cathodes.

1 | Introduction

The global transition toward electric vehicles (EVs), driven by the imperative to achieve "carbon peak and carbon neutrality", is advancing at an unprecedented pace worldwide [1]. However, given the relatively limited lifespan of 5–8 years for Li-ion batteries (LIBs), this paradigm shift foreshadows a looming challenge: the tidal wave of end-of-life LIBs is coming soon [2–4]. Among the mainstream cathode materials, olivine-structured $LiFePO_4$ (LFP) has garnered dominant market share in the electric vehicle market due to its compelling advantages, including low cost, superior safety, and long cycle life [5, 6]. Nevertheless, the

Xutao Liang and Ran Wang contributed equally to this work.

degradation of LFP cathodes is inevitable, typically manifesting as a capacity fade below 80% of the initial value, which renders them inadequate for EV applications [7–9]. The projected exponential growth in spent LFP batteries over the next decade underscores an urgent need for efficient recycling methods. Without sustainable management, these batteries not only represent a substantial waste of valuable resources but also pose severe environmental threats, highlighting the necessity of developing advanced recycling technologies.

Conventional recycling strategies, predominantly pyrometallurgical and hydrometallurgical processes, focus on the extraction of valuable metal elements [10, 11]. Unfortunately, pyrometallurgy is inherently energy-intensive, operates at extremely high temperatures, and generates hazardous off-gases from the combustion of organic components (such as: binders and graphite) [12]. Hydrometallurgy, while less energy-consuming, relies heavily on corrosive chemical reagents and produces enormous volumes of acidic wastewater and solid residues, raising significant environmental concerns [13, 14]. More fundamentally, both strategies destroy the valuable cathode microstructure, resulting in low economic viability for LFP recycling and a failure to recover the high value-added material function [15, 16]. Consequently, direct regeneration has emerged as a promising alternative in recent years. This strategy aims to directly restore the electrochemical performance of spent LFP (S-LFP) by remedying its intrinsic degradation issues and structural defects, thereby preserving the original structure as much as possible and offering a path of upcycling with maximal economic and environmental benefits [17, 18].

It is widely known that the degradation of LFP primarily stems from two interconnected factors: the loss of active Li and the resultant formation of crystal and surface defects. Lithium ion depletion not only triggers the transformation of Fe(II) to Fe(III) but also leads to the formation of Fe-Li antiferromagnetic defects. This cation disordering disrupts the one-dimensional Li^+ diffusion channels along the [010] direction and causes lattice distortion. Simultaneously, repeated cycling accumulates internal stress, potentially leading to particle cracking and electrical contact loss [19, 20]. Therefore, an ideal regeneration process must simultaneously replenish Li, revert Fe(III) to Fe(II), eliminate the anti-site defects, and restore the structural/surface integrity [21]. However, current direct regeneration methods still face significant practical hurdles. The conventional solid-state calcination strategy, which involves mixing S-LFP with Li sources (*e.g.*: Li_2CO_3) and reductants (*e.g.*: sucrose), suffers from inefficient solid-solid contact, leading to incomplete and non-uniform repair [22]. Moreover, many strategies focus solely on defect repair within the bulk crystal structure, neglecting the equally critical aspect of restoring the electronic conductivity of the material, that is, surface/interface, which is often compromised by the loss of the carbon coating during cycling or regeneration [23, 24].

Herein, we propose an efficient and scalable strategy direct regeneration strategy that employs methionine as a multifunctional reagent to concurrently address the challenges of bulk crystal repair and surface interface engineering. Methionine, a low-cost, environmentally benign amino acid, acts as an electron donor via its hydroxyl group, which serves a dual purpose: (1) as a potent reductant to efficiently reduce Fe(III) to Fe(II) and eliminate Fe-Li anti-site defects, thereby recuperating the Li^+ diffusion pathways; (2) as a single-source precursor for in situ formation of a N/S-doped conductive interface during a subsequent mild annealing process. This multifunctional conductive interface significantly enhances electronic conductivity and bolsters the structural stability of the regenerated LFP [25, 26]. As a result, the regenerated LFP exhibits a high discharge capacity of 150.76 mAh g^{-1} and a capacity retention rate of >87% after 800 cycles, rivaling that of its commercial counterpart. This work demonstrates a simple, scalable, and sustainable pathway for the upcycling of spent LFP cathodes in the green recycling of LIBs.

2 | Results and Discussion

2.1 | Direct Regeneration Strategy for Structural Restoration and Interface Construction

The degradation of spent $LiFePO_4$ (S-LFP) is primarily governed by the loss of active Li and the consequent formation of Fe(III) phases and Fe—Li anti-site defects, which collectively impede Li^+ diffusion and degrade electrical contact. Therefore, eliminating these defects is crucial for restoring the electrochemical performance of LFP. However, the formation of Fe(III) within the crystal structure significantly increases electrostatic repulsion between iron ions and surrounding atoms, which hinders the return of iron ions to their original positions within the crystal lattice. To address these issues simultaneously, we designed a direct regeneration strategy using methionine as a multifunctional reagent in conjunction with lithium acetate (CH_3COOLi) as the Li source. As shown in Figure 1, this strategy enables a one-step sintering process that not only replenishes Li and repairs crystal defects but also constructs a stable N/S-doped carbon coating on the R-LFP. Methionine, an economical small-molecule amino acid containing both amino and sulfide groups, plays a dual role in this process. First, it acts as an effective electron donor, reducing Fe(III) to Fe(II) and eliminating Fe—Li anti-site defects, thereby restoring the original $LiFePO_4$ crystal framework and reopening Li^+ migration pathways. Second, it serves as a single-source precursor for the in situ formation of an N/S-doped carbon layer interface during annealing. This interface significantly enhances electronic conductivity, while the heteroatom doping optimizes the surface electronic structure, thereby improving charge transfer kinetics.

The structural recovery during the regeneration process was first confirmed by x-ray diffraction (XRD). As shown in Figure 2a, the distinct $FePO_4$ phase observed in the S-LFP pattern completely disappeared after regeneration, and the XRD profile of R-LFP aligned well with that of commercial $LiFePO_4$ (C-LFP), indicating successful phase restoration. Meanwhile, to improve the repair efficiency of S-LFP, multiple experiments were carried out at different annealing temperatures to determine the optimal annealing temperature (Figure S1). With the rise of annealing temperature, the peak profiles of $LiFePO_4$ are optimally restored at 650°C, and further elevating the temperature brings limited improvement to the structural recovery of the material. Elemental contents of S-LFP and R-LFP were determined using inductively coupled plasma (ICP) analysis, which was shown in Figure 2b. The Li/Fe molar ratio of S-LFP was calculated to be 0.978, below the theoretical stoichiometric ratio of 1.0 for LFP,

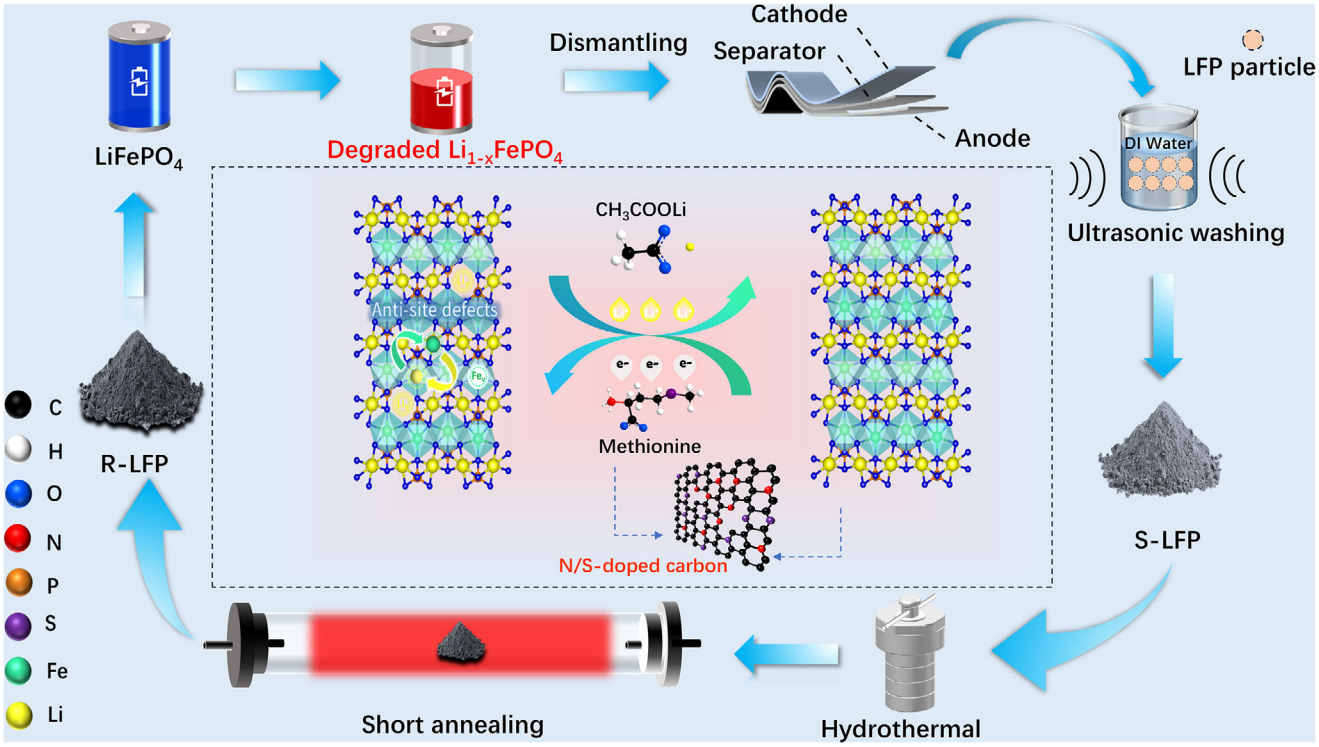

FIGURE 1 | Mechanism of LFP degradation and its direct regeneration strategy.

signifying substantial Li loss attributable to side reactions (*e.g.*: transition metal dissolution triggering electrolyte oxidation and decomposition) and solid electrolyte interphase (SEI) formation. After regeneration, the Li/Fe ratio recovered to 1.023, even slightly surpassing that of C-LFP (1.013, Table S1), confirming effective Li replenishment.

Subsequently, x-ray photoelectron spectroscopy (XPS) was employed to determine the chemical state and local environment of iron. As shown in Figure 2c, for the S-LFP, the peaks at 712.8 and 710.5 eV can be attrobuted to Fe(III) and Fe(II) in the Fe $2p_{1/2}$ band, respectively, indicating a dominant Fe(III) signal. However, Fe(II) became the predominant species in the R-LFP. Meanwhile, the ratio of fitted areas for the Fe $2p_{3/2}$ peaks indicated a higher abundance of Fe(III) on the S-LFP surface compared to the R-LFP surface [27]. Depth-profiling XPS analysis provided further insight, which was shown in Figure 2d,e. For the S-LFP, the Fe $2p_{3/2}$ peak at 711.3 eV was attributed to the Fe(III) phase. With increasing etching time, the Fe $2p_{3/2}$ peak gradually shifted toward 710.4 eV, indicating the emergence of degraded regions from within the particles [28]. However, the chemical state of Fe in R-LFP remained uniform as Fe(II) throughout, demonstrating the thoroughness of the reduction process mediated by methionine. Further evidence for the successful reduction of Fe(III) was obtained from Fe K-edge x-ray absorption near-edge structure (XANES) spectroscopy(Figure 2f). The absorption edge of R-LFP shifted to a lower energy compared to S-LFP, confirming the reduction of iron to a lower average valence state. Correspondingly, the extended x-ray absorption fine structure (EXAFS) spectra (Figure 2g–i) showed that the Fe—O bond length in R-LFP increased and approached the standard value for pristine LFP (~2.0 Å). The decreased intensity of the Fe—O scattering peak in R-LFP suggested a reduction in the coordination number of oxygen around Fe atoms, consistent with the conversion from Fe(III)O_6 to Fe(II)O_6 octahedra [29, 30]. These results collectively confirmed that the methionine-based regeneration strategy effectively restores the chemical composition, crystal structure, and local coordination environment of the S-LFP.

2.2 | Morphological Evolution and Structural Restoration

The microstructure and deep phase transitions before and after regeneration were characterized using HRTEM and SEM. As shown in Figure 3a, the surface of S-LFP was covered with an irregular and partially detached carbon coating, likely resulting from prolonged cycling. In stark contrast, a uniform and continuous N/S-doped carbon layer was observed on R-LFP (Figure 3d), which was crucial for enhancing electronic conductivity. Correspondingly, SEM images revealed that S-LFP particles exhibited severe surface cracks resulting from prolonged cycling-induced stress (Figure 3b). And these cracks were effectively healed after the regeneration process (Figure 3e), which can be attributed to the particle reconstruction and defect repair that occurred during the transient annealing, leading to a more integrated morphology. Compared with S-LFP, regenerated $LiFePO_4$ exhibits obviously weakened particle agglomeration, thereby greatly boosting the electronic conductivity of the cathode material (Figure S2). At the same time, the atomic-resolution analysis of S-LFP identified lattice fringes of 0.2345 nm, corresponding to the (012) plane of the electrochemically inactive $FePO_4$ (FP) phase, confirming the presence of irreversible degradation (Figure 3g). Conversely, the HRTEM image of R-LFP displayed well-defined lattice fringes

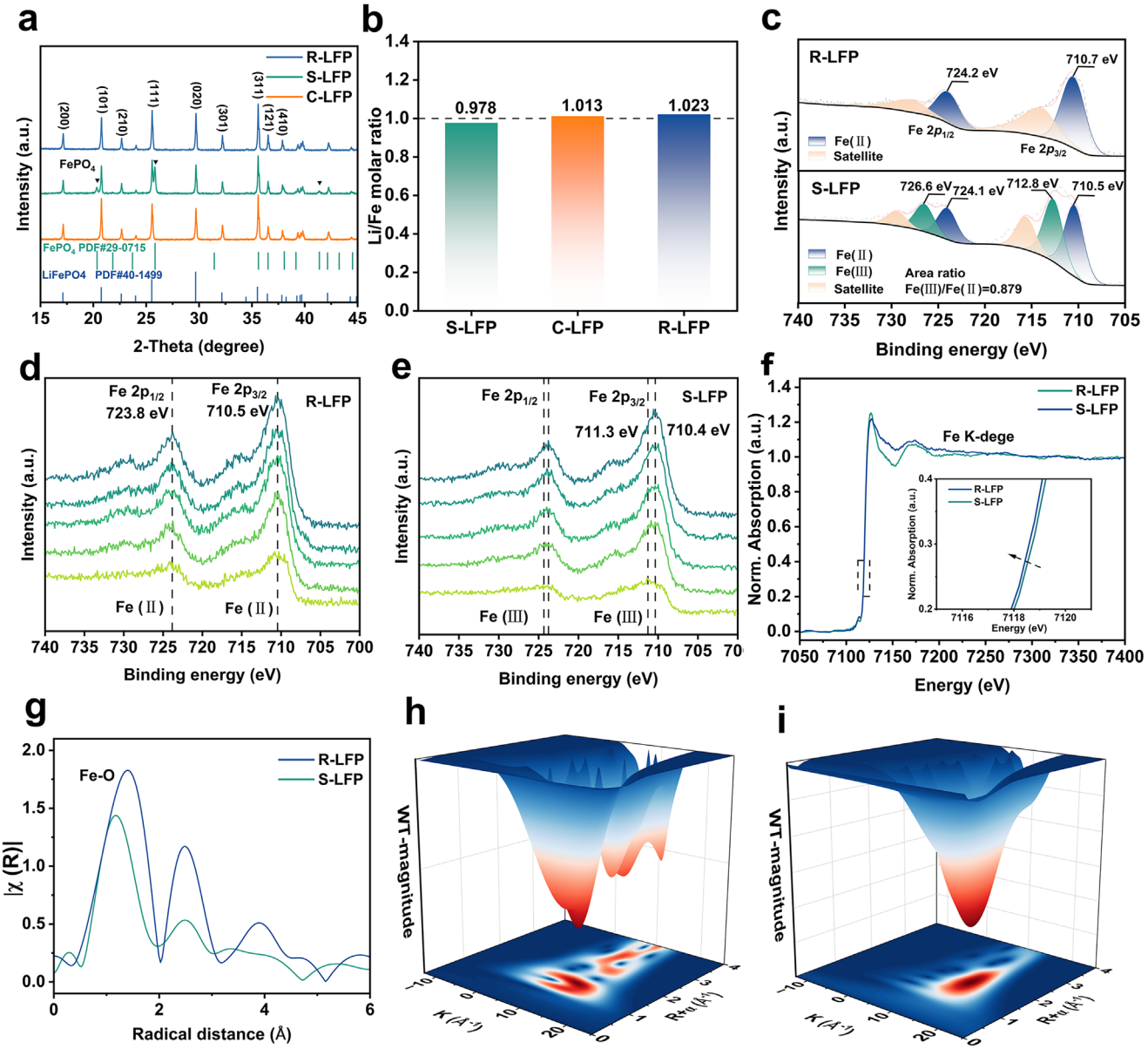

FIGURE 2 | Structural restoration of S-LFP. (a) XRD patterns of S-LFP and R-LFP. (b) Li/Fe molar ratios calculated from ICP results. (c) Fe 2p XPS spectra of R-LFP and S-LFP. (d,e) Fe 2p XPS spectra of R-LFP and S-LFP by in-depth etching. (f) Fe K-edge XANES spectra. (g) EXAFS fitting curves of R-LFP and S-LFP in R-space (h,i) Wavelet transform analysis of Fe-K edge for R-LFP and S-LFP.

with a spacing of 0.3695 nm (Figure 3h), matching the (101) plane of the olivine $LiFePO_4$ structure, signaling the recovery of the electrochemically active phase.

Moreover, the Fast Fourier Transform (FFT) patterns from selected areas provided complementary evidence. The disordered speckles in the FFT pattern of S-LFP indicated the presence of amorphous or severely defective regions (Figure 3c). After regeneration, the FFT pattern of the corresponding area in R-LFP exhibited sharp, ordered diffraction spots (Figure 3f), unequivocally demonstrating the restoration of a well-crystallized structure. Finally, elemental mapping via HAADF-STEM and EDS confirmed the homogeneous distribution of the fundamental constituents (C, O, Fe, P) throughout the R-LFP particles (Figure 3i). Importantly, the nitrogen and sulfur signals were co-localized and evenly distributed, verifying the successful formation of a uniform N/S-doped carbon coating. The quantitative analysis indicated doping levels of 0.57 wt.% for N and 0.07 wt.% for S (Table S2). This conductive and N/S-doped carbon layer played a pivotal role in enhancing the overall electrical conductivity and interfacial stability of R-LFP.

2.3 | Improved Electrochemical Performance and Enhanced Reaction Kinetics

The efficacy of the direct regeneration strategy was unequivocally confirmed by comprehensive electrochemical evaluations. The galvanostatic charge-discharge profiles of R-LFP exhibited a significantly reduced voltage hysteresis compared to S-LFP (Figure 4a), indicating lower polarization and improved reaction

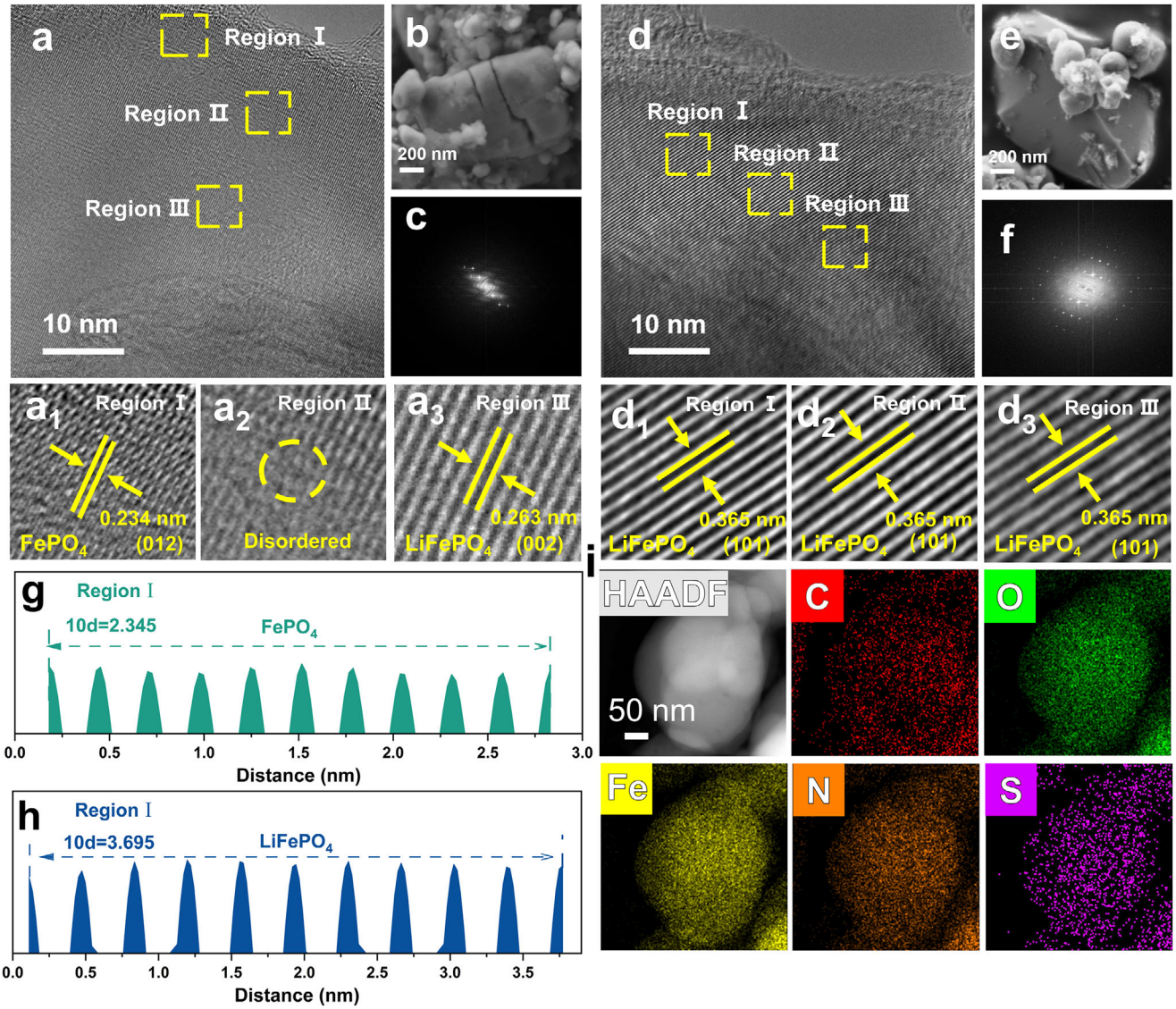

FIGURE 3 | Microstructure characterization and depth phase analysis before and after regeneration. (a) HRTEM images of the S-LFP with the corresponding magnified views (a_1–a_3) of the boxed regions. (b) SEM images of the S-LFP and the scale bar is 200 nm. (c) corresponding FFT pattern of S-LFP. d) HRTEM images of the R-LFP with the corresponding magnified views (d_1–d_3). (e) SEM images of R-LFP and the scale bar is 200 nm. (f) corresponding FFT pattern of R-LFP. (g,h) Lattice fringe analysis of S-LFP and R-LFP, respectively. (i) HAADF-STEM images and corresponding EDS elemental maps of R-LFP.

kinetics. This was further corroborated by cyclic voltammetry (CV) measurements, which was shown in Figure 4b. The oxidation and reduction peaks near 3.2 and 3.6 V corresponded to the Fe (II)/Fe(III) redox pair, and R-LFP showed sharper and more symmetric Fe^{2+}/Fe^{3+} redox peaks with a smaller voltage separation, underscoring the high reversibility (Figure S3). Furthermore, the rate performance of R-LFP was remarkably superior to that of S-LFP across various current densities (Figure 4c). Specifically, R-LFP delivered high specific capacities of 154.4 and 91.1 mAh g^{-1} at 0.1 C and 10 C, respectively, significantly outperforming S-LFP (124.9 mAh g^{-1} at 0.1 C and 63.5 mAh g^{-1} at 10 C) and even comparable to that of C-LFP (Figure S4). This enhanced rate performance was attributed to the restored crystal structure and the highly conductive N/S-doped carbon coating, which facilitated rapid electron transport and Li^+ diffusion.

Then, the Li^+ diffusion coefficient was quantitatively analyzed using CV at various scan rates (Figure 4d,e and Figure S5) and the Randles-Sevcik equation [31, 32].

$$I_p = \left(2.65 \times 10^5\right) n^{3/2} S\, D_{Li}{}^{1/2}\, C_{Li} v^{1/2} \quad (1)$$

In this equation, Ip, n, S, D_{Li}, and C_{Li} represent the peak current, electrode surface area, Li^+ diffusion coefficient, electrode surface area, concentration of Li^+ participating in the redox reaction, and scan rate, respectively. When parameters (n, S, C_{Li}) are constant, the slope of the Li^+ diffusion coefficient ($D_{Li}{}^+$) versus electrode surface area, $I_p/\nu^{1/2}$, is observed. As shown in Figure 4f and Figure S6, the steeper slope of the peak current versus the square root of the scan rate ($\nu^{1/2}$) plot for R-LFP confirmed a faster Li^+ diffusion rate, a direct consequence of the repaired Li^+ channels and eliminated anti-site defects.

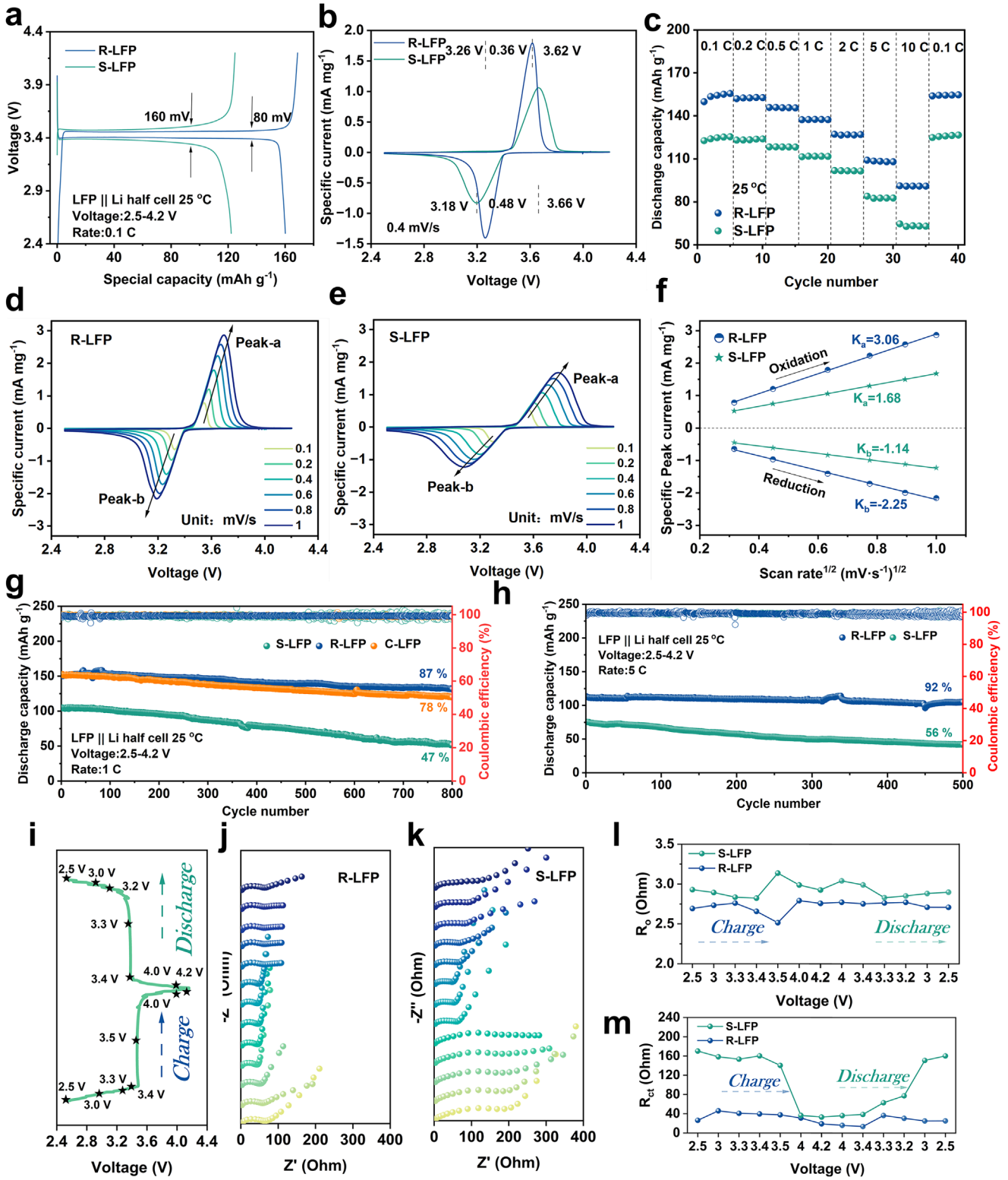

FIGURE 4 | Electrochemical performance and kinetics. (a) Initial charge and discharge curves of S-LFP and R-LFP at 0.1 C. (b) CV curves measured at a scanning rate of 0.1 mV s^{-1} of S-LFP and R-LFP. (c) Rate performance of S-LFP and R-LFP. (d,e) CV curves of S-LFP and R-LFP at scan rates from 0.1 to 1.0 mV s^{-1}. (f) Linear relationship between the peak current and the square root of the scan rate for Li^+ diffusion coefficient calculation. (g) Long-term cycling performance at 1.0 C. (h) Cyclic performance at a high rate of 5.0 C. (i) Voltage profile for the in situ EIS measurements. (j,k) Nyquist plots of R-LFP and S-LFP during the first charge–discharge processes. (l,m) The fitted values of R_{ct} and R_o value of S-LFP and R-LFP.

The long-term cycling stability of R-LFP was also exceptionally promising. As shown in Figure 4g, R-LFP retained >87% of its initial capacity after 800 cycles at 1.0 C, a performance comparable to commercial LFP and far exceeding that of S-LFP (47%). From the long-cycle charge–discharge curves at 1.0 C (Figure S7), we can also observe that R-LFP exhibits lower and more stable polarization voltage compared with S-LFP. Even under a high rate of 5.0 C, it still maintained >92% capacity retention after 500 cycles (Figure 4h and Figure S8). Similarly, even at a high rate of 10.0 C, R-LFP still possesses superior cycling stability in comparison with S-LFP (Figure S9). This outstanding stability can be ascribed to the robust N/S-doped carbon layer, which not only enhances electrical contact but also stabilizes the particle surface, suppressing side reactions with the electrolyte, which is consistent with EXAFS and CV results. To gain deeper insight into the interfacial kinetics, in situ electrochemical impedance spectroscopy (EIS) was performed at various states of charge (Figure 4i). The corresponding equivalent circuit models were shown in Figure S10, with fitting results for S-LFP and R-LFP impedance parameters presented in Tables S3 and S4. Notably, during charging, the charge transfer resistance (R_{ct}) gradually decreases due to enhanced conductivity in the LFP cathode during de-lithiation. During discharging, this process reverses, with resistance slightly increasing before stabilizing. Nevertheless, at various test potentials, the charge transfer resistance (R_{ct}) of R-LFP is consistently lower than that of S-LFP and even comparable to C-LFP. (Figure 4j,k and Figure S11), reflecting a more facile charge transfer process at the electrode-electrolyte interface. Furthermore, the R_{ct} of R-LFP showed minimal variation with voltage (Figure 4l,m), indicating the formation of a stable and conductive cathode-electrolyte interphase (CEI) on the regenerated, structurally sound particles. In contrast, the large potential-dependent fluctuation of R_{ct} in S-LFP suggested an unstable interface, likely due to its defective crystal structure and surface cracks [33, 34].

2.4 | Regeneration Mechanism Analysis

As mentioned above, the methionine exhibits multiple functions in the regeneration of S-LFP. It can serve as a unique multifunctional agent, acting simultaneously as a potent reductant and a single-source precursor for the construction of N/S doped interface. The electron-donating functional groups (—COOH, —NH_2) in methionine effectively reduce Fe(III) to Fe(II), thereby eliminating the detrimental Fe-Li anti-site defects. This critical step not only restores the crystallographic integrity but also reopens the one-dimensional Li^+ diffusion channels along the [010] direction [35, 36]. Concurrently, during subsequent annealing, methionine decomposes to in situ form a uniform and dense N/S-doped carbon layer interface, which heals surface cracks and establishes a highly conductive network.

Then, the direct regeneration mechanism of S-LFP is elucidated through a combination of structural and spectroscopic techniques. As shown in Figure 5a,b, rietveld refinement of the XRD patterns quantitatively confirmed the structural recovery (Tables S5 and S6), while both S-LFP and R-LFP exhibited the Pnma space group. The Rietveld refinement results showed low Rp and Rwp values (Tables S7 and S8), confirming the reliability of the repair [37].

The S-LFP cathode exhibited a high anti-site defect concentration of 4.7% and a significant $FePO_4$ (FP) phase fraction of 21.81%, which was consistent with the ICP-OES results. After regeneration, the FP phase was entirely eliminated in R-LFP, and the anti-site defect density was drastically reduced to 1.6%, unequivocally demonstrating the efficacy of the process in healing the bulk crystal structure. At the same time, spectroscopic analyses provided further evidence at the molecular level. As shown in Figure 5c, Raman spectroscopy revealed obvious P-O bond vibrations in S-LFP, while the attenuated intensity in R-LFP indicated that Li supplementation successfully suppressed FP phase formation and repaired lattice defects. And compared to S-LFP (0.94), the I_D/I_G ratio for R-LFP (0.85) decreased, indicating the restoration of a more graphitized and conductive carbon coating through the regeneration process [38, 39]. Regeneration process enhanced the graphitization of surface carbon layer, which was beneficial for improving the rate performance. The FTIR spectra revealed a shift of the characteristic peaks toward lower wavenumbers for R-LFP (Figure 5d), which was attributed to the reduced lattice strain and diminished influence of Fe-Li defects on the PO_4 tetrahedra—consistent with refined XRD data [40].

During regeneration, N and S element doping strengthened the Fe-O and P-O bonds at the R-LFP interface. XPS analysis confirmed the successful incorporation, which was shown in Figure 5e–g. In the C 1s spectrum of R-LFP, the peak at 285.4 eV corresponded to C—N, C—S, and C—O bonds, while the S 2p spectrum exhibited the characteristic peaks at 163.28 and 166.48 eV, attributed to S—S and S—C bonding configurations, respectively. Furthermore, in the N 1s spectrum, pyridine-N and pyrrole-N species were identified at 398.53 and 399.74 eV, respectively, providing additional confirmation of N atom doping. This N/S co-doping interface was crucial as it enhanced the electronic conductivity and strengthened the Fe—O and P—O bonds, thereby improving the structural stability [41, 42].

The impact of this regeneration on the electrochemical kinetics was conclusively demonstrated by Relaxation time distribution (DRT) and Gradient Intermittent Titration (GITT) analyses. The DRT profile of R-LFP displayed a significant suppression of the characteristic peaks associated with charge transfer (R_{ct}) and Li^+ diffusion through the CEI (R_{CEI}) compared to S-LFP (Figure 5h,i and Figures S12 and S13), indicating drastically improved interfacial kinetics [43, 44]. The contour maps of CV curves for S-LFP and R-LFP were plotted to better understand the reversibility of cathode structure and enhancement of Li^+ migration kinetics during regenerated R-LFP cycling, with a sweep range of 0.1–1 mV s^{-1} and a voltage window of 2.5 – 4.2 V (Figure 5j,k and Figure S14) [45, 46]. S-LFP experiences clear phase separation and inhomogeneous phase transition throughout a long cycling process, which leads to an asymmetric half-peak width (0.3 V for the oxidized peaks and 0.39 V for the reduced peaks). In comparison, R-LFP displays a similar half-peak width (0.16 V), implying that the highly reversible electrochemical reaction of R-LFP during the cycling procedure. This was further supported by GITT measurements, where the overpotential required for Li^+ plating/stripping was substantially lower for R-LFP (Figure 5l), directly correlating with the reduction of Fe-Li defects and the restoration of facile Li^+ diffusion pathways (Figure S15).

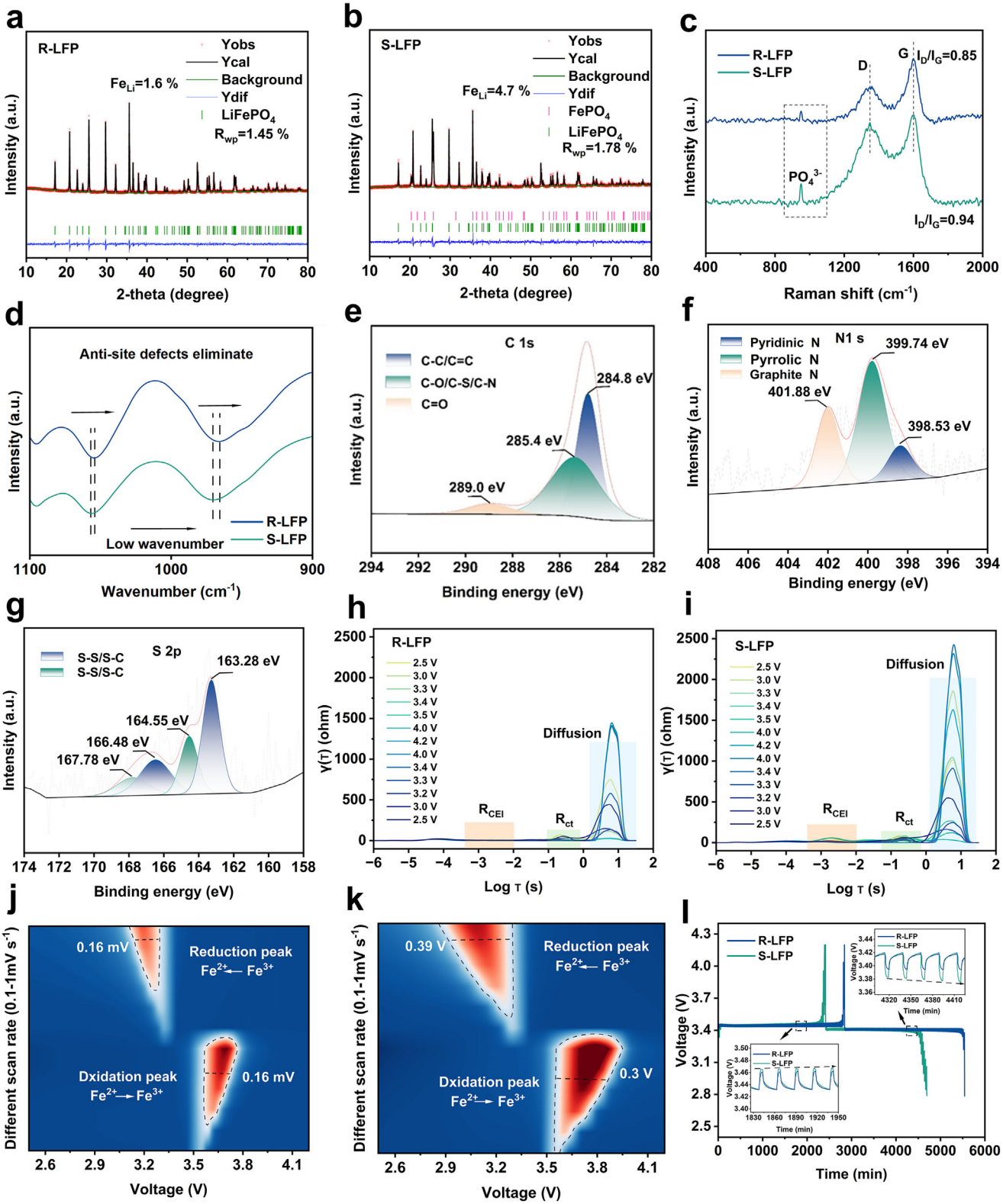

FIGURE 5 | Regeneration mechanism analysis. (a,b) XRD patterns and corresponding Rietveld refinement results of R-LFP (a) and S-LFP (b). (c) Raman spectra of R-LFP and S-LFP. (d) FTIR spectra of R-LFP and S-LFP. (e–g) XPS spectra of C 1s, N 1s and S 2p for R-LFP, confirming the chemical environment of the N/S-doped carbon layer. (h,i) DRT analysis of R-LFP and S-LFP. (j,k) Contour plots of CV curves of R-LFP and S-LFP at different scan rates. (l) GITT tests for R-LFP and S-LFP during charging/discharging.

Collectively, these results delineated a coherent mechanism whereby methionine orchestrated a direct regeneration, concurrently rectifying bulk crystal defects and constructing a N/S-doped conductive interface, ultimately leading to the full recovery of electrochemical performance.

3 | Conclusion

In summary, we have developed and validated a direct regeneration strategy for S-LFP cathodes using methionine as a multifunctional reagent. This approach simultaneously accomplishes defect repair in the bulk crystal and the construction of a conductive N/S-doped carbon interface. The methionine-mediated process effectively reduces Fe(III) to Fe(II), eliminates Fe-Li anti-site defects, and replenishes the Li content, thereby restoring the one-dimensional Li^+ diffusion channels. Concurrently, the in situ formed N/S-doped carbon layer significantly enhances electronic conductivity, suppresses detrimental side reactions, and strengthens the interfacial Fe—O and P—O bonds, leading to improved structural integrity. Benefiting from these synergistic effects, the R-LFP exhibits improved electrochemical performance, including a high specific capacity (150.76 mAh g^{-1} at 1.0 C), remarkable rate capability, and outstanding long-term cycling stability (87% capacity retention after 800 cycles), a performance comparable to commercial LFP. The effectiveness of this regeneration mechanism is unequivocally confirmed through a suite of characterization techniques, including XPS, DRT, and GITT analysis, which collectively verify the improved kinetics and structural stability. This work provides fundamental insights into the direct regeneration mechanism and presents a practical solution with significant potential to enhance the economic viability and environmental sustainability of battery recycling.

Acknowledgements

This work was supported by the National Natural Science Foundation of China (No. 22402146, 22572140, U24A6002), the Beijing Natural Science Foundation Xiaomi innovation joint Foundation (L223011), Young Elite Scientists Sponsorship Program by CAST (2022QNRC001), Shanxi energy internet research institute (SXEI2023A004), Open Research Fund of Guangdong Advanced Carbon Materials Co., Ltd. (Kargen-2024B0905), the special fund for Science and Technology Innovation Teams of Shanxi Province (202204051001004), State Key Laboratory of Flexible Electronics Key Task Research Project (ZS030ZR25012).

Conflicts of Interest

The authors declare no conflict of interest.

Data Availability Statement

The data that support the findings of this study are available from the corresponding author upon reasonable request.

References

1. G. Harper, R. Sommerville, E. Kendrick, et al., "Recycling Lithium-ion Batteries From Electric Vehicles," *Nature* 575 (2019): 75–86, https://doi.org/10.1038/s41586-019-1682-5.

2. J. Baars, T. Domenech, R. Bleischwitz, H. E. Melin, and O. Heidrich, "Circular Economy Strategies for Electric Vehicle Batteries Reduce Reliance on Raw Materials," *Nature Sustainability* 4 (2021): 71–79, https://doi.org/10.1038/s41893-020-00607-0.

3. F. Degen, M. Winter, D. Bendig, and J. Tübke, "Energy Consumption of Current and Future Production of Lithium-ion and Post Lithium-ion Battery Cells," *Nature Energy* 8 (2023): 1284–1295, https://doi.org/10.1038/s41560-023-01355-z.

4. K. Jia, G. Yang, Y. He, et al., "Degradation Mechanisms of Electrodes Promotes Direct Regeneration of Spent Li-Ion Batteries: A Review," *Advanced Materials* 36 (2024): 2313273, https://doi.org/10.1002/adma.202313273.

5. R. Malik, "The Secret Life of $LiFePO_4$ Particles," *Joule* 2 (2018): 2204–2205, https://doi.org/10.1016/j.joule.2018.11.005.

6. J. Ni, M. Morishita, Y. Kawabe, M. Watada, N. Takeichi, and T. Sakai, "Hydrothermal Preparation of $LiFePO_4$ Nanocrystals Mediated by Organic Acid," *Journal of Power Sources* 195 (2010): 2877–2882, https://doi.org/10.1016/j.jpowsour.2009.11.017.

7. M. Wang, K. Liu, S. Dutta, et al., "Recycling of Lithium Iron Phosphate Batteries: Status, Technologies, Challenges, and Prospects," *Renewable and Sustainable Energy Reviews* 163 (2022): 112515, https://doi.org/10.1016/j.rser.2022.112515.

8. B. Li, B. Zhang, X. Bai, et al., "A Dynamic Self-Healing Protective Layer Enabling Stable Zinc Ion Batteries Through Strong Zn-S Affinity and Intramolecular Hydrogen Bonding," *Angewandte Chemie International Edition* 64 (2025): 2465807, https://doi.org/10.1002/anie.202503345.

9. Y. Guo, Y. Yao, C. Guo, et al., "Atomistic Observation and Transient Reordering of Antisite Li/Fe Defects Toward Sustainable $LiFePO_4$," *Energy & Environmental Science* 17 (2024): 7749–7761, https://doi.org/10.1039/d4ee01622j.

10. N. Vieceli, C. A. Nogueira, C. Guimarães, M. F. C. Pereira, F. O. Durão, and F. Margarido, "Hydrometallurgical Recycling of Lithium-ion Batteries by Reductive Leaching With Sodium Metabisulphite," *Waste Management* 71 (2018): 350–361, https://doi.org/10.1016/j.wasman.2017.09.032.

11. J. Neumann, M. Petranikova, M. Meeus, et al., "Recycling of Lithium-Ion Batteries—Current State of the Art, Circular Economy, and Next Generation Recycling," *Advanced Energy Materials* 12 (2022): 2102917, https://doi.org/10.1002/aenm.202102917.

12. B. Makuza, Q. Tian, X. Guo, K. Chattopadhyay, and D. Yu, "Pyrometallurgical Options for Recycling Spent Lithium-ion Batteries: A Comprehensive Review," *Journal of Power Sources* 491 (2021): 229622, https://doi.org/10.1016/j.jpowsour.2021.229622.

13. X. Chen, H. Ma, C. Luo, and T. Zhou, "Recovery of Valuable Metals From Waste Cathode Materials of Spent Lithium-ion Batteries Using Mild Phosphoric Acid," *Journal of Hazardous materials* 326 (2017): 77–86, https://doi.org/10.1016/j.jhazmat.2016.12.021.

14. M. Shan, K. Wei, L. Cheng, et al., "Toward Sustainable Graphite Anode Recycling: From Degradation Understanding to Targeted Regeneration," *Nano Research Energy* 5 (2026): 9120230, https://doi.org/10.26599/nre.2026.9120230.

15. J. J. Roy, S. Rarotra, V. Krikstolaityte, et al., "Green Recycling Methods to Treat Lithium-Ion Batteries E-Waste: A Circular Approach to Sustainability," *Advanced Materials* 34 (2021): 2103346, https://doi.org/10.1002/adma.202103346.

16. Y. Yang, E. G. Okonkwo, G. Huang, S. Xu, W. Sun, and Y. He, "On the Sustainability of Lithium Ion Battery Industry—A Review and Perspective," *Energy Storage Materials* 36 (2021): 186–212, https://doi.org/10.1016/j.ensm.2020.12.019.

17. Y.-M. Li, Y. He, K. Jia, et al., "The Weakened Super-Exchange Interaction Realizes the Direct Regeneration of Spent Lithium-Ion Battery Cathodes," *Angewandte Chemie International Edition* 64 (2025): 2520448, https://doi.org/10.1002/anie.202520448.

18. R. Fu, B. Zhang, T. Lu, et al., "A Dilute and Non-flammable Electrolyte Engineering Enables Stable SEI for Low-temperature Zinc Batteries," *Energy Storage Materials* 80 (2025): 104374, https://doi.org/10.1016/j.ensm.2025.104374.

19. S. Lei, W. Sun, and Y. Yang, "Comprehensive Technology for Recycling and Regenerating Materials From Spent Lithium Iron Phosphate Battery," *Environmental Science & Technology* 58 (2024): 3609–3628, https://doi.org/10.1021/acs.est.3c08585.

20. Z. Zeng, P. Xu, J. Li, et al., "Large-Scale and Homogenized Strategies of Spent $LiFePO_4$ Recycling: Reconstruction of Targeted Lattice," *Advanced Functional Materials* 34 (2023): 2308671, https://doi.org/10.1002/adfm.202308671.

21. G. R. Gardiner and M. S. Islam, "Anti-Site Defects and Ion Migration in the $LiFe_{0.5}Mn_{0.5}PO_4$Mixed-Metal Cathode Material," *Chemistry of Materials* 22 (2009): 1242–1248, https://doi.org/10.1021/cm902720z.

22. E. N. Falah, Widyastuti, L. Noerochim, et al., "A Study of the Addition of G-C_3N_4 in Direct Regeneration of Spent $LiFePO_4$ Battery Cathodes on the Electrochemical Performance of Lithium-ion Batteries (LIB)," *Materials Research Bulletin* 187 (2025): 113378, https://doi.org/10.1016/j.materresbull.2025.113378.

23. J. Zhang, S. L. Zhang, N. N. Tham, et al., "Efficient Direct Regeneration of Spent $LiFePO_4$ From Various Degradation States for Sustainable Battery Recycling," *Chemical Communications* 61 (2025): 8375–8378, https://doi.org/10.1039/d5cc01308a.

24. Q. Jing, J. Zhang, Y. Liu, W. Zhang, Y. Chen, and C. Wang, "Direct Regeneration of Spent $LiFePO_4$ Cathode Material by a Green and Efficient One-Step Hydrothermal Method," *ACS Sustainable Chemistry & Engineering* 8 (2020): 17622–17628, https://doi.org/10.1021/acssuschemeng.0c07166.

25. J. Shen, S. Shang, X. Chen, D. Wang, and Y. Cai, "Highly Fluorescent N, S-co-doped Carbon Dots and Their Potential Applications as Antioxidants and Sensitive Probes for Cr (VI) Detection," *Sensors and Actuators B: Chemical* 248 (2017): 92–100, https://doi.org/10.1016/j.snb.2017.03.123.

26. M. Kasif, A. Alarifi, M. Afzal, and A. Thirugnanasambandam, "N, S-codoped Carbon Dots for Antioxidants and Their Nanovehicle Potential as Molecular Cargoes," *RSC Advances* 14 (2024): 32041–32052, https://doi.org/10.1039/d4ra05994h.

27. A. Adamson, K. Tuul, T. Bötticher, S. Azam, M. D. L. Garayt, and M. Metzger, "Improving Lithium-ion Cells by Replacing Polyethylene Terephthalate Jellyroll Tape," *Nature Materials* 22 (2023): 1380–1386, https://doi.org/10.1038/s41563-023-01673-3.

28. D. Tang, G. Ji, J. Wang, et al., "A Multifunctional Amino Acid Enables Direct Recycling of Spent $LiFePO_4$ Cathode Material," *Advanced Materials* 36 (2023): 2309722, https://doi.org/10.1002/adma.202309722.

29. D. Xu, P. Wang, and B. Shen, "Synthesis and Characterization of Sulfur-doped Carbon Decorated $LiFePO_4$ Nanocomposite as High Performance Cathode Material for Lithium-ion Batteries," *Ceramics International* 42 (2016): 5331–5338, https://doi.org/10.1016/j.ceramint.2015.12.064.

30. C. Feng, Y. Cao, L. Song, et al., "Direct Regeneration of Industrial $LiFePO_4$ Black Mass Through a Glycerol-Enabled Granule Reconstruction Strategy," *Angewandte Chemie International Edition* 64 (2024): 2418198, https://doi.org/10.1002/anie.202418198.

31. R. Wang, X. Chen, Z. Huang, et al., "Twin Boundary Defect Engineering Improves Lithium-ion Diffusion for Fast-charging Spinel Cathode Materials," *Nature Communications* 12 (2021): 2536972, https://doi.org/10.1038/s41467-021-23375-7.

32. Y.-L. Cao, Z. Chen, P. Liu, and Y.-L. Xie, "N Doping Promotes the Multiplication Capability and Cycling Stability of Cobalt-free Lithium-rich Layered Cathode Materials," *Journal of Power Sources* 661 (2026): 238623, https://doi.org/10.1016/j.jpowsour.2025.238623.

33. U. Nisar, N. Muralidharan, R. Essehli, R. Amin, and I. Belharouak, "Valuation of Surface Coatings in High-Energy Density Lithium-ion Battery Cathode Materials," *Energy Storage Materials* 38 (2021): 309–328, https://doi.org/10.1016/j.ensm.2021.03.015.

34. K. Jia, J. Ma, J. Wang, et al., "Long-Life Regenerated $LiFePO_4$ From Spent Cathode by Elevating the D-Band Center of Fe," *Advanced Materials* 35 (2022): 2208034, https://doi.org/10.1002/adma.202208034.

35. P. Xu, Q. Dai, H. Gao, et al., "Efficient Direct Recycling of Lithium-Ion Battery Cathodes by Targeted Healing," *Joule* 4 (2020): 2609–2626, https://doi.org/10.1016/j.joule.2020.10.008.

36. J. Wang, B. Tan, D. Chen, et al., "Multifunctional N, S-co-Doped Carbon Quantum Dots Enable Defect Healing and Conductive Network Construction in Spent $LiFePO_4$ Cathodes," *Chemical Engineering Journal* 522 (2025): 167249, https://doi.org/10.1016/j.cej.2025.167249.

37. T. Wang, C. Gao, Z. Zheng, et al., "N-Doped Carbon Layer Construction and Targeted Defect Repair Enables Direct Regeneration of Spent $LiFePO_4$ Cathodes," *Advanced Functional Materials* 35 (2025): 2502930, https://doi.org/10.1002/adfm.202502930.

38. J. Wu, G. K. P. Dathar, C. Sun, et al., "In Situ Raman Spectroscopy of $LiFePO_4$: Size and Morphology Dependence During Charge and Self-discharge," *Nanotechnology* 24 (2013): 424009, https://doi.org/10.1088/0957-4484/24/42/424009.

39. Y. Lin, T. Wang, C. Gao, et al., "Direct and Low-Temperature Regeneration of Degraded $LiFePO_4$ Cathodes at Ambient Conditions Using Green and Sustainable Deep Eutectic Solvent," *Advanced Science* 12 (2025): 2504683, https://doi.org/10.1002/advs.202504683.

40. Y. Wang, J. Zhang, J. Xue, X. Ke, and G. Liang, "$LiFePO_4$/C Composites With High Compaction Density as Cathode Materials for Lithium-ion Batteries With High Volumetric Energy Density," *Ionics* 27 (2021): 4687–4694, https://doi.org/10.1007/s11581-021-04078-x.

41. N. Shaji, F. Jiang, J. Y. Sung, et al., "Heteroatoms-doped Carbon Effect on $LiFePO_4$ Cathode for Li-ion Batteries," *Journal of Energy Storage* 72 (2023): 108710, https://doi.org/10.1016/j.est.2023.108710.

42. Y. Liu, W. Tu, J. Bai, et al., "Amino Group-Aided Efficient Regeneration Targeting Structural Defects and Inactive $FePO_4$ Phase for Degraded $LiFePO_4$ Cathodes," *Small* 20 (2024): 2405362, https://doi.org/10.1002/smll.202405362.

43. Y. Liu, J. Bai, R. Shi, et al., "Direct Recycling of Degraded $LiFePO_4$ Cathode Material via Natural Electron Donors Healing and Targeted Surface Reconstruction," *Advanced Materials* 36 (2025): 2511246, https://doi.org/10.1002/adma.202511246.

44. S. Liu, B. Wu, X. Bai, et al., "A Solvent-Induced Solid Polymer Electrolyte With Controllable Polymerization for Low-Temperature Lithium Metal Batteries," *Nano Letters* 25 (2025): 5241–5249, https://doi.org/10.1021/acs.nanolett.4c06471.

45. S. Zhang, Y. Liu, G. Chen, et al., "Adaptive Localized Ectopic Structure Enhances Regeneration of Spent Lithium-Ion Battery Cathodes," *Advanced Materials* 32 (2025): 2513547, https://doi.org/10.1002/adma.202513547.

46. L. Cheng, M. Shan, Y. Wang, et al., "Achieving Stable and Fast Ion Transport in Regenerated $LiFePO_4$ Via Vacancy-Mediated Upcycling," *Angewandte Chemie International Edition* 65 (2026): 24847, https://doi.org/10.1002/anie.202524847.

Supporting Information

Additional supporting information can be found online in the Supporting Information section.

Supporting File: smll74994-sup-0001-SuppMat.docx.